Petroleum Science (2021) 18:530–545
https://doi.org/10.1007/s12182-020-00533-y

ORIGINAL PAPER

Performance of free gases during the recovery enhancement of shale gas by CO_2 injection: a case study on the depleted Wufeng–Longmaxi shale in northeastern Sichuan Basin, China

Jun Liu[1] · Ling-Zhi Xie[1,2] · Bo He[1] · Peng Zhao[2] · Huai-Yu Ding[3]

Received: 23 July 2020 / Accepted: 4 November 2020 / Published online: 27 November 2020
© The Author(s) 2020

Abstract
In this work, a novel thermal–hydraulic–mechanical (THM) coupling model is developed, where the real geological parameters of the reservoir properties are embedded. Accordingly, nine schemes of CO_2 injection well (IW) and CH_4 production well (PW) are established, aiming to explore the behavior of free gases after CO_2 is injected into the depleted Wufeng–Longmaxi shale. The results indicate the free CH_4 or CO_2 content in the shale fractures/matrix is invariably heterogeneous. The CO_2 involvement facilitates the ratio of free CH_4/CO_2 in the matrix to that in the fractures declines and tends to be stable with time. Different combinations of IW–PWs induce a difference in the ratio of the free CH_4 to the free CO_2, in the ratio of the free CH_4/CO_2 in the matrix to that in the fractures, in the content of the recovered free CH_4, and in the content of the trapped free CO_2. Basically, when the IW locates at the bottom Wufeng–Longmaxi shale, a farther IW–PWs distance allows more CO_2 in the free phase to be trapped; furthermore, no matter where the IW is, a shorter IW–PWs distance benefits by getting more CH_4 in the free phase recovered from the depleted Wufeng–Longmaxi shale. Hopefully, this work is helpful in gaining knowledge about the shale-based CO_2 injection technique.

Keywords CO_2 geological sequestration · Enhanced shale gas recovery · Free gas · Wufeng–Longmaxi Formation · THM coupled modeling

1 Introduction

Current knowledge strongly supports CO_2 sequestration in geological formations (e.g., shale and coalbed) as a promising approach to respond to the issue of excessive anthropogenic CO_2 emissions into the atmosphere, which is treated as carbon-negative technology and thus has been receiving growing attention (Abidoye et al. 2015; Zhang et al. 2015; Wan and Liu 2018; Liu et al. 2020; Rani et al. 2020; Řimnáčová et al. 2020). Therein, injecting CO_2 into shale reservoirs is becoming increasingly attractive and has been lauded as a win–win solution for meeting geological CO_2 storage and simultaneous enhanced gas recovery (CS-EGR) from shales (Liu et al. 2017b, 2019a, b; Kalra et al. 2018; Pan et al. 2018; Yang et al. 2019; Zhang et al. 2020). However, understanding of shale-based CS-EGR is limited, with only few pilot field studies undertaken, in which strategy optimization, site characterization/monitoring, and hazard assessment & management need to be taken into account in a comprehensive manner (Chi et al. 2017; Ajayi et al. 2019; Zhang et al. 2019; Chen et al. 2020; Iddphonce et al. 2020). In other words, despite being proven to be a feasible technique, CS-EGR in the shale is not yet mature enough for full national or worldwide deployment.

To promote the development of the shale-based CS-EGR technique, considerable work has been organized, in which significant achievements have been drawn (Iddphonce et al. 2020). For example, it has been proven that the CO_2–CH_4 displacement behavior differs in the shales from different sedimentary environments (Du et al. 2019). Another example is that the CS-EGR efficiency is considerably affected by

Edited by Yan-Hua Sun

✉ Peng Zhao
scu_zhaopeng@163.com

[1] State Key Laboratory of Hydraulics and Mountain River Engineering, Institute of New Energy and Low-Carbon Technology, Sichuan University, Chengdu 610065, China

[2] College of Architecture and Environment, Sichuan University, Chengdu 610065, China

[3] Liaohe Oilfield Company, PetroChina, Panjin 124010, China

the CO_2 proportion in the injected CO_2–N_2 mixture (Li and Elsworth 2019). In one other example, NMR-based investigation indicated that the properties (e.g., mineral composition) of shale reservoir can interfere with the CS-EGR outputs (Liu et al. 2019b). However, the examples mentioned above mainly pay attention to the gases (CO_2/CH_4) in the adsorbed phase during the CO_2–CH_4 interaction, in which the performance of the free gases (CO_2/CH_4) tends to be ignored. Unfortunately, neglecting the free gases in the process of shale-based CS-EGR does not exist in isolation and even is a common phenomenon reported in many literatures (Liu et al. 2017b; Zhou et al. 2019; Římnáčová et al. 2020).

Although the competitive adsorption of CO_2/CH_4 is the primary element enabling CS-EGR in shales (Wang et al. 2018b; Liu et al. 2019a), the gases in free phase inevitably appear to the spaces of the pores and fractures in shale reservoirs during the CO_2–CH_4 interaction (Fathi and Akkutlu, 2014). Basically, free gas is crucial for shale gas exploration/exploitation and even occupies over 50% of in situ gas content in shales (Liu et al. 2016b). To separately study the multiphase (free/adsorbed) gas in shales, experimental approaches have been conducted, and sound achievements have been made. For instance, isotopic geochemistry (Liu et al. 2016b) and low-field NMR (Yao et al. 2019) were successfully introduced to quantitatively identify the CH_4 in the free and adsorbed phase. Nevertheless, it was found that a single experimental methodology was usually performed at a restricted scale, and could hardly recognize the free CO_2 and free CH_4 from the CO_2–CH_4 mixture at the same time during the dynamic CO_2–CH_4 interaction in shales. Given this situation, physics-based numerical simulations can be employed to address concerns about the free gases during the shale-based CS-EGR process, in which multi-factors can be investigated in a clear and transparent manner.

Up to a point, numerical attempts have given rise to knowledge improvement on the performance of free gases during the CS-EGR operation in shales. There are two examples; one is that numerical work advocated that the portion of free gas is always less than that of adsorbed gas in the process of CO_2–CH_4 interplay in shales, under variable reservoir permeability and temperature/pressure (Mohagheghian et al. 2019). Another modeling study has suggested that an increase in the ratio of the free CH_4 to adsorbed CH_4 would decrease the CO_2 sequestration potential of the Utica shale formation (Tao et al. 2014). Unfortunately, current simulations about free CH_4/CO_2 in shales are usually run with a plain mathematical model with only a single layer or/and isotropic conditions being simulated, which is contrary to field fact that multilayer and heterogeneous characteristics exist extensively in shale reservoirs (Tang et al. 2016; Liu et al. 2017a). For this reason, limited existing numerical achievements can be directly generalized and carried out in a real shale formation that usually has a thickness of tens to several hundred meters, where vertical heterogeneity emerges in many reservoir parameters, such as the porosity/permeability, the Langmuir volume, and Young's modulus (Tang et al. 2016; Liu et al. 2017a). Clearly, the development of a comprehensive model that contains as many realistic conditions as possible is, therefore, the need of the hour, aiming to enhance understanding of the free gases behavior during the CS-EGR process in shales.

In this work, because the Wufeng–Longmaxi Formation in the northeastern Sichuan Basin (SW China) has huge potential resources of shale gas (Liu et al. 2017a), it is selected for simulation where the CS-EGR technique has the opportunity to be implemented. Accordingly, a thermal–hydraulic–mechanical (THM) coupled model is developed using the COMSOL Multiphysics software, attempting to simulate the depleted condition of the Wufeng–Longmaxi shale. Herein, this integrated model not only contains the responses of the rock deformation, competitive CH_4/CO_2 sorption, gas/water two-phase flow, and thermal expansion in the dual-porosity system but also involves the real heterogeneity of the reservoir properties of the Wufeng–Longmaxi shale. Using a mathematical approach, this work focuses on the dynamic interaction of free CO_2 and free CH_4 during the continuous CO_2 injection into the depleted Wufeng–Longmaxi shale, with a run time of roughly 30 years (10,000 d). Accordingly, in a quantitative manner, a series of simulations are set to clarify the anisotropic content variation of free gases (CO_2 and CH_4) in the modeling reservoir, under different relative locations of the CO_2 injection well (IW) and the CH_4 production well (PW). Furthermore, the strengths and weaknesses of each IW–PWs combo are also discussed, in terms of the different desired objectives. Hopefully, the peculiar perspectives from the gases in the free phase during the CO_2–CH_4 interaction in shales will help to deepen awareness on the potential field deployment of the CS-EGR project in the shale reservoir.

2 Geological background

In this work, the case Wufeng–Longmaxi shale is from the Well-WQ2 that is a shale gas exploration well and is located in the northeastern Sichuan Basin, Southwest (SW) China (Fig. 1a). In this region, an arc tectonic belt system with a thrust belt trending to the southwest was formed by a series of tectonic activities, in which the Chengkou-Fangxian and Shashi Buried fault zones are quintessential examples (Li et al. 2013; Ji et al. 2015; Liu et al. 2017a).

Figure 1b shows the continuous sedimentary succession in the study area from the late Sinian to the Cenozoic Era, except for the missing strata from the Devonian to the Carboniferous period (Meng and Zhang 2000; Shi et al. 2012; Li et al. 2013). Under this sedimentary background, previous

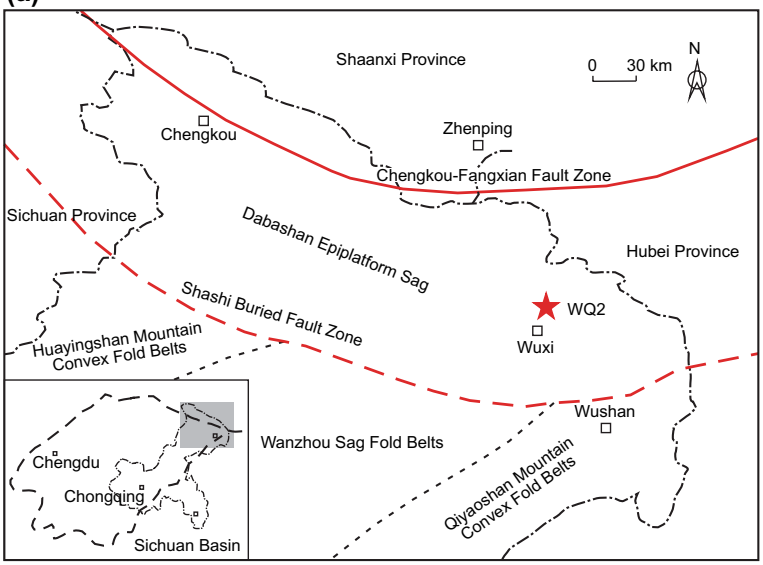

(b)

Stratigraphy System	Stratigraphy Formation	Lithology	HC system
Jurassic	Baitianba	Sandstone, mudstone basal conglomerate	
Triassic	Xujiahe	Mudstone coal beds sandstone	
	Leikoupo	Gypsum, halite limestone	Seal beds
	Jialingjiang	Gypsum, halite dolomite	Seal beds
	Tongjiezi	Oolitic limestone	Reservoir beds
	Feixianguang	Bioclastic limestone dolostone	Reservoir beds
Permian	Changxing	Bioclastic limestone	Reservoir beds
	Wujiaping	Mudstone, coal beds limestone	Source rocks
	Maokou	Chert-bearing limestone	Source rocks
	Qixia	Limestone mudstone	Source rocks
Silurian	Cuijiagou	Siltstone, shale	Seal beds
	Longmaxi	Shale	Seal beds
Ordovician	Wufeng	Mudstone, siltstone	Seal beds
	Baota	Limestone	Reservoir beds
Cambrian	Sanyoudong	Oolitic dolostone	Reservoir beds
	Qinjiamiao	Limestone	Reservoir beds
	Shipai	Dolostone	Reservoir beds
	Guojiaba	Carbonaceous mudstone	

Upper hydrocarbon system

Lower hydrocarbon system

(c)

Layer No.	Depth, m	*E*, GPa	*v*, 10^{-1}	*φ*, %		*k*, 10^{-18} m²		V_L, m³/t		P_L, MPa	
				φ_m	φ_f	k_h	k_v	$V_{L\text{-}CH_4}$	$V_{L\text{-}CO_2}$	$P_{L\text{-}CH_4}$	$P_{L\text{-}CO_2}$
1	1200–1210	44.4	2.27	3.54	0.51	4.20	4.12	4.12	10.68	4.12	10.68
2	1210–1220	45.6	2.70	2.78	0.32	1.82	3.84	3.84	8.75	3.84	8.75
3	1220–1230	51.5	2.52	2.07	0.43	3.20	3.58	3.58	8.69	3.58	8.69
4	1230–1240	63.8	2.08	2.84	0.66	4.60	3.04	3.04	9.50	3.04	9.50
5	1240–1250	62.4	2.13	1.36	0.44	1.68	2.28	2.28	11.75	2.28	11.75
6	1250–1260	60.7	2.19	2.88	0.42	6.40	3.16	3.16	8.79	3.16	8.79
7	1260–1270	60.9	2.18	1.72	0.53	5.00	2.60	2.60	13.99	2.60	13.99
8	1270–1280	61.3	2.17	5.54	0.66	8.10	3.21	3.21	10.09	3.21	10.09
9	1280–1290	58.6	2.26	1.26	0.51	3.80	2.87	2.87	9.11	2.87	9.11
10	1290–1300	57.8	2.29	2.59	0.78	3.60	4.01	4.01	6.01	4.01	6.01

HC-hydrocarbon system; *E*-Young's modulus; *v*-Poisson's ratio; *φ*-Porosity; φ_f-Fracture porosity; φ_m-Matrix porosity; *k*-Permeability; k_h-Horizontal permeability; k_v-Vertical permeability; V_L-Langmuir volume P_L-Langmuir pressure

Fig. 1 Geological background of Well-WQ2 and the vertical heterogeneous reservoir characteristics (Shi et al. 2012; Li et al. 2013; Zhu et al. 2016; Liu et al. 2017a; Zhao et al. 2020). **a** Geological information of the Northeastern Sichuan Basin. **b** Integrated stratigraphic column of the Northeastern Sichuan Basin. **c** Vertical heterogeneity of the Wufeng–LongMaxi shales in the WQ2 shale well

studies have identified two conventional hydrocarbon source systems (Fig. 1b): the bottom one (from the Cambrian Guojiaba Formation to the Silurian Cuijiagou Formation) and the upper one (from the Permian Qixia Formation to the Triassic Leikoupo Formation) (Li et al. 2013; Liu et al. 2017a). Therein, during the shale gas exploration and exploitation, the Wufeng–Longmaxi shale is usually treated as a close combination due to the conformable contact relationship between the upper Ordovician Wufeng Formation and the lower Silurian Longmaxi Formation (Zhu et al. 2016; Ye et al. 2017; Wang et al. 2018a).

The Wufeng–Longmaxi shale in the Well-WQ2 has a thickness of roughly 100 m with a buried depth of 1200–1300 m, where the bottom section (about 10 m) belongs to the Wufeng shale (Liu et al. 2016a, 2017a). At such a buried depth, the depleted pressure of the Wufeng–Longmaxi shale is estimated at about 1.7 MPa (Zhang et al. 2015). Statistics suggest that the vertical heterogeneity is strong in the involved Wufeng–Longmaxi shale which also has anisotropic characteristics in the reservoir properties (e.g., porosity/permeability) (Liu et al. 2016a, 2017a) (Fig. 1c). In addition, the well logs of Well-WQ2 indicate the temperature of the Wufeng–Longmaxi shale is 36 °C (310 K), the water saturation is 0.3, and the in-situ stresses in the horizontal and vertical directions are 30 MPa and 36 MPa, respectively (Zhao et al. 2020). Such field data provide a basis for the model development in this numerical work, ensuring this model is as close to the real formation conditions as possible.

3 Development of the mathematical model

3.1 Model description for the Wufeng–Longmaxi shale

Figure 2a exhibits the schematic of the simulation model in this work, which is treated as a typical pattern and contains

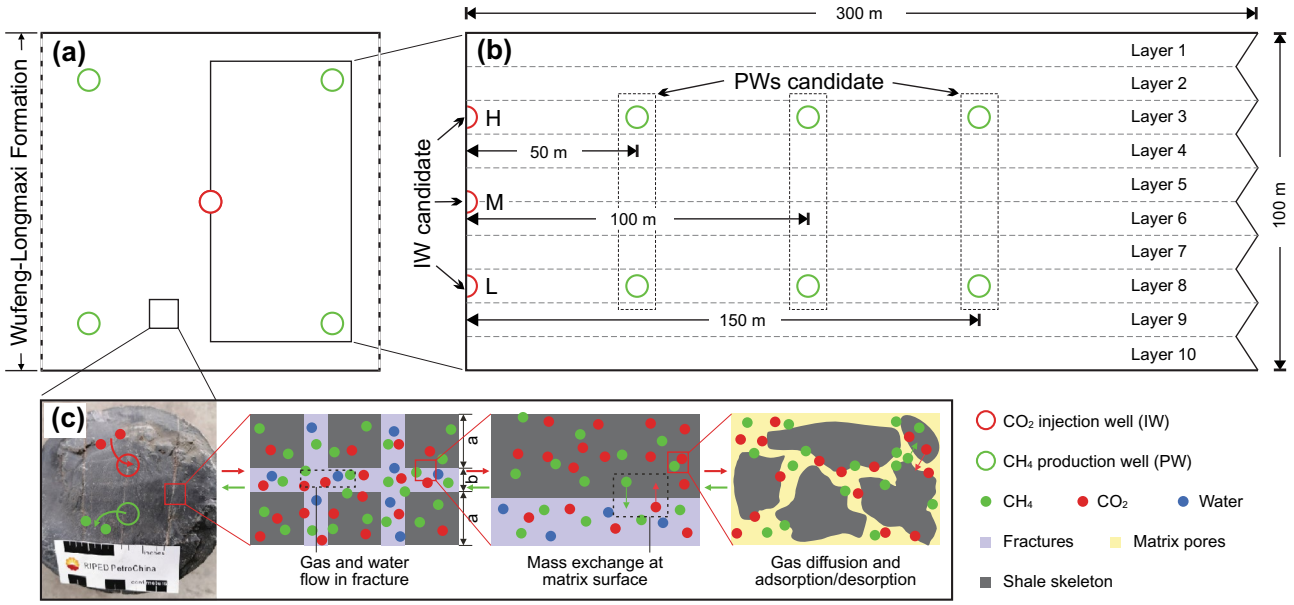

Fig. 2 Schematic diagram of the process of CS-EGR in a shale reservoir (Zhao et al. 2020). All involved wells have a radius of 0.1 m. **a** Typical pattern of IW–PWs. **b** Relative locations of IW–PWs. **c** Mass transport of multi-fluids in the shale

one injection well (IW) in the center and four production wells (PWs) in the corners (Li and Elsworth 2019). This pattern is axisymmetric, so a two-dimensional representative is selected for the numerical simulation (Fig. 2b). According to the geological parameters, the model height is determined as 100 m and is equally divided into ten sections to reveal the vertical heterogeneity of the reservoir properties. The model width is set 300 m to avoid possible influence of the right boundary condition (e.g., formation overpressure) (Li et al. 2017). Accordingly, the simulation area of 100 m × 300 m is divided into 5085 elements, and all boundaries are airtight for flux, except for the right boundary with the initial gas pressure being set. As the CS-EGR operation is conducted in the depleted conditions of the Wufeng–Longmaxi shale, the initial pressure of the simulative reservoir is set as 2 MPa (that is, 0.3 MPa for CO_2 and 1.7 MPa for CH_4). In this modeling process, under a temperature of 305 K, constant pressures of 0.1 MPa and 7 MPa are applied to the PWs and IW during the CS-EGR process, respectively. To develop the mathematical model, the primary parameters (see "Appendix") are obtained from the existing literatures (Dahaghi 2010; Sun et al. 2013; Fathi and Akkutlu 2014; Li and Elsworth 2015, 2019; Fan et al. 2019a, b, c; Ma et al. 2020; Zhao et al. 2020), while the key heterogeneous information on the Wufeng–Longmaxi shale is derived from real fieldwork (Fig. 1).

As shown in Fig. 2b, three IW candidates and three PWs candidates are organized to investigate how the relative locations of IW and PWs affect the free gas behavior of the CS-EGR operation in shales. Among these nine IW–PWs combos, when the IW is located at the lower section and is 50 m far away from the PWs in the horizontal direction, the modeling case is labeled as L50. In a similar fashion, the rest of the cases are marked as L100, L150, M50, M100, M150, H50, H100, and H150, respectively (Fig. 2). Herein, the layer 3, interface of layers 5–6, and layer 8, where the IW candidate is set, represent the upper, middle, and lower sections of the simulative shale reservoir, respectively.

3.2 THM coupling process and governing equations

Since many parameters are involved in this simulation work (see "Appendix"), CS-EGR in shales is identified as a complicated process and involves integral feedback in the THM coupling phenomenon. Basically, the hydraulic field contains complex mass transport of binary gases (CO_2/CH_4) with the gas–water represented as two-phase flows superposed on competitive non-isothermal adsorption (Fig. 2c). Once the shale reservoir captures the nonthermally equilibrated CO_2, heat transfer, such as thermal conduction/convection, occurs among the CH_4, CO_2, water, and shale skeleton, which is accompanied by energy release/adsorption associated with gas adsorption/desorption, in turn impacting on the thermal field (Fan et al. 2019a). Furthermore, the dynamic variation in the hydraulic and thermal fields can interfere with the mechanical field (e.g., shrink/swelling of the shale matrix), influencing the anisotropic porosity/permeability and thus affecting the convective fluxes of the water, gas, and energy (Fan et al. 2019a).

The shale reservoir in this work is described as a dual-porosity media (Fig. 2c), which is used extensively in previous numerical works (Bandis et al. 1983; Nassir et al. 2014; Li and Elsworth 2015, 2019; Zhou et al. 2018; Zhao et al. 2020). According to these works above, a series of governing equations representing rock deformation, competitive CH_4/CO_2 sorption, gas/water two-phase flow, and thermal expansion are used for the CS-EGR model development in this work.

4 Results and discussion

In the dual-porosity media, fractures and matrix pores are the internal spaces of shale for trapping free gases (CO_2/CH_4). In this work, four types of free gases are classified to investigate the behavior of free CO_2/CH_4 during the CS-EGR process in the depleted Wufeng–Longmaxi shale—CH_4 in the fracture, CO_2 in the fracture, CH_4 in the matrix and CO_2 in the matrix. Accordingly, this work separately studies the performance of free CH_4 or free CO_2, and then the dynamic interaction between free CH_4 and free CO_2 during the recovery enhancement of shale gas by CO_2 injection into the depleted Wufeng–Longmaxi shale, under variable IW–PWs locations. Note that this numerical model's thickness value is 1 m when the gas content is calculated, where the involved gas content indicates the content of gas in free phase.

4.1 Content variation of free CH_4 during shale-based CS-EGR process

Prior to the involvement of the injected CO_2, the original content of free CH_4 both in the fracture and in the matrix is strongly heterogeneous in the vertical direction, where the free CH_4 in the matrix is visibly more than that in fracture (Fig. 3). This heterogeneous tendency is similar to the vertical variation of the fracture/matrix porosity of the Wufeng–Longmaxi shale shown in Fig. 1, owing to the free gas content being directly determined by the free space under the depleted reservoir pressure. Once the CO_2 injection starts, the content variation of the free CH_4 in the fracture/matrix occurs. Taking M100 as an example, it is found that the free CH_4 in the fracture continuously varies during the CS-EGR process, intuitively reflecting the accumulation of free CH_4 in the left side of the PWs and the decrease in that in the right side of the PWs (Fig. 4a). For the same case, the cloud pictures qualitatively indicate an overall reduction of free CH_4 in the matrix over time after CO_2 is injected into the shale reservoir (Fig. 4b). These variations address the concept that the CO_2 injection can facilitate the migration of free CH_4 in the depleted Wufeng–Longmaxi shale reservoir.

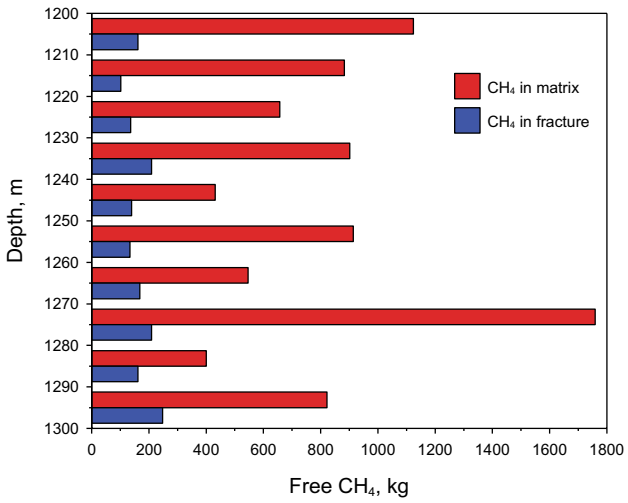

Fig. 3 Original free CH_4 content in modeling reservoir of the depleted Wufeng–Longmaxi shale

After a production period of 10,000 d, the CS-EGR operation enables the content difference of free CH_4 in the fracture/matrix under variable IW–PWs combos. According to the cloud pictures, at a fixed IW location, a farther IW–PWs distance in the horizontal direction makes more CH_4 in the free phase trapped in the shale fracture and matrix after 10,000 d of CS-EGR operation (Fig. 5a, b). Comparatively, when PWs are located as fixed, there are less obvious changes for the free CH_4 in the shale fracture/matrix along with the variation of the IW location. Anyhow, after 10,000 d of CS-EGR production, the vertical heterogeneity emerges for all outputs of free CH_4 under different IW–PWs relative locations (Fig. 5a, b).

To further display the heterogeneous characteristics of free CH_4 in the Wufeng–Longmaxi shale, the content variation of free CH_4 in each layer is concluded at different points in time during the CS-EGR process. As shown in Fig. 6, the free CH_4 content in each layer is dramatically affected by the relative locations of IW–PWs. A shorter IW–PWs distance (fixed IW location) makes the CO_2 injection-induced decrement of the free CH_4 content greater, which is more obvious for the layers near the IW. Besides, when the PWs location is fixed, a smaller decrement goes to the free CH_4 content in the layers close to the IW. Moreover, in some operating cases, the content decrement is negative for the free CH_4 in the layers near IW (e.g., Fig. 6a–c, e, f, h, i), revealing that the CO_2 injection facilitates the increment of free CH_4 in shale fractures at the initial CS-EGR phase. Taking H150 as an example, the free CH_4 content in the fracture of layer 1 first increases and then decreases (Fig. 7a), while that of layer 8 decreases monotonously (Fig. 7b), after CO_2 is injected. This phenomenon is caused by the content variation of free CH_4 in the matrix. Using the same example of

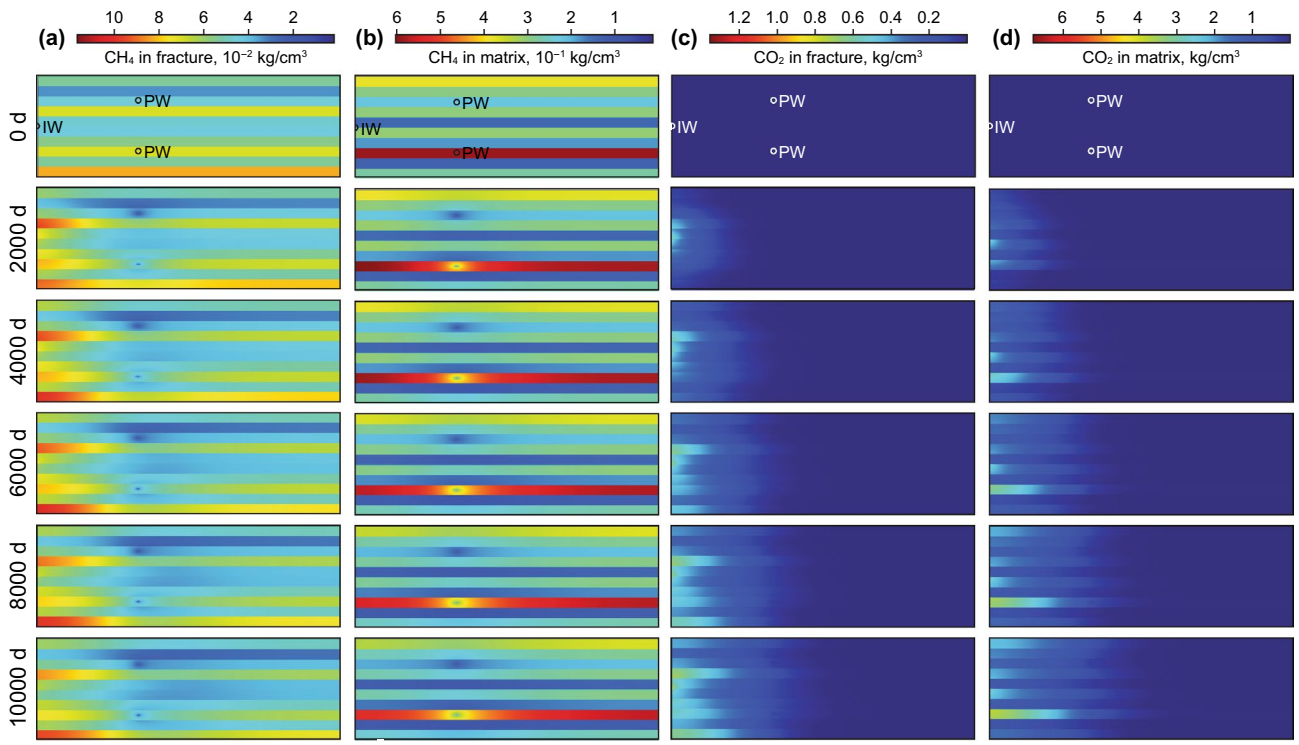

Fig. 4 Content variation of free gases during the CS-EGR process over time for the representative case M100

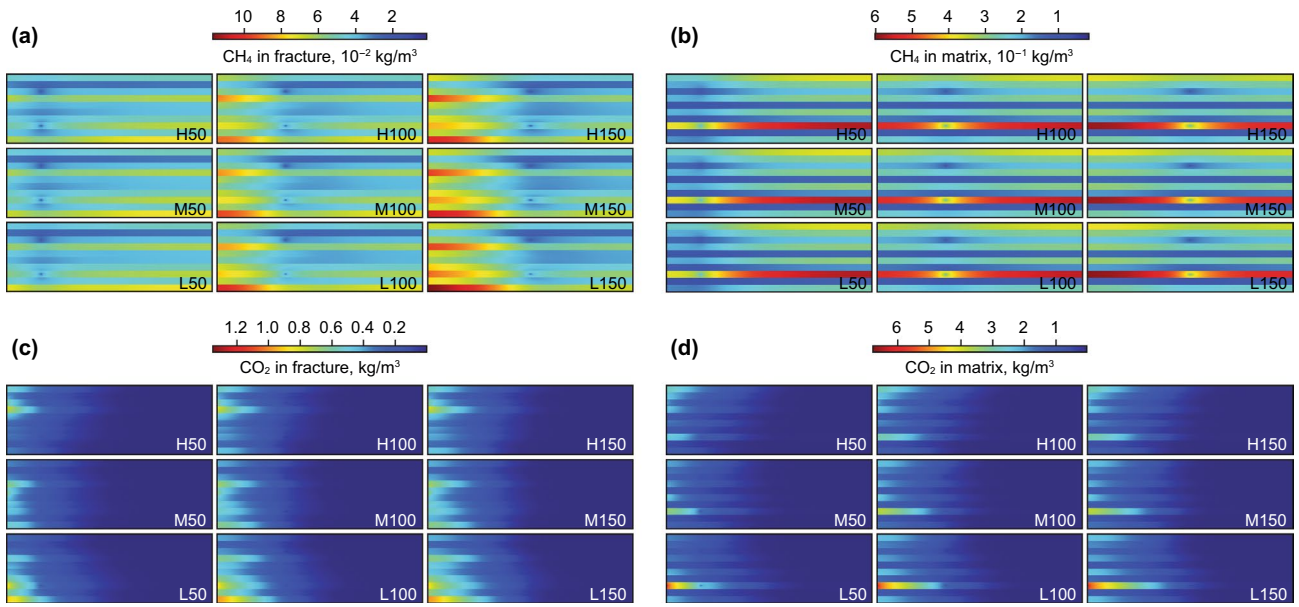

Fig. 5 Free gases content after 10,000 d CS-EGR operation under different IW–PWs conditions

H150, the massive accumulation of free CH_4 in the matrix, caused by the displacement of the adsorbed CH_4 by CO_2 injection, allows the release of the free CH_4 in the matrix into the fracture, regarding layer 1 which is close to the IW location (Fig. 7a). Comparatively, for layer 8 of H150, the decrease of free CH_4 in the fracture/matrix is monotonic and mainly controlled by the release of CH_4 pressure in the shale reservoir (Fig. 7b).

With regard to the mass of CH_4 in the matrix, its decrement varies in a heterogeneous way for all layers, under

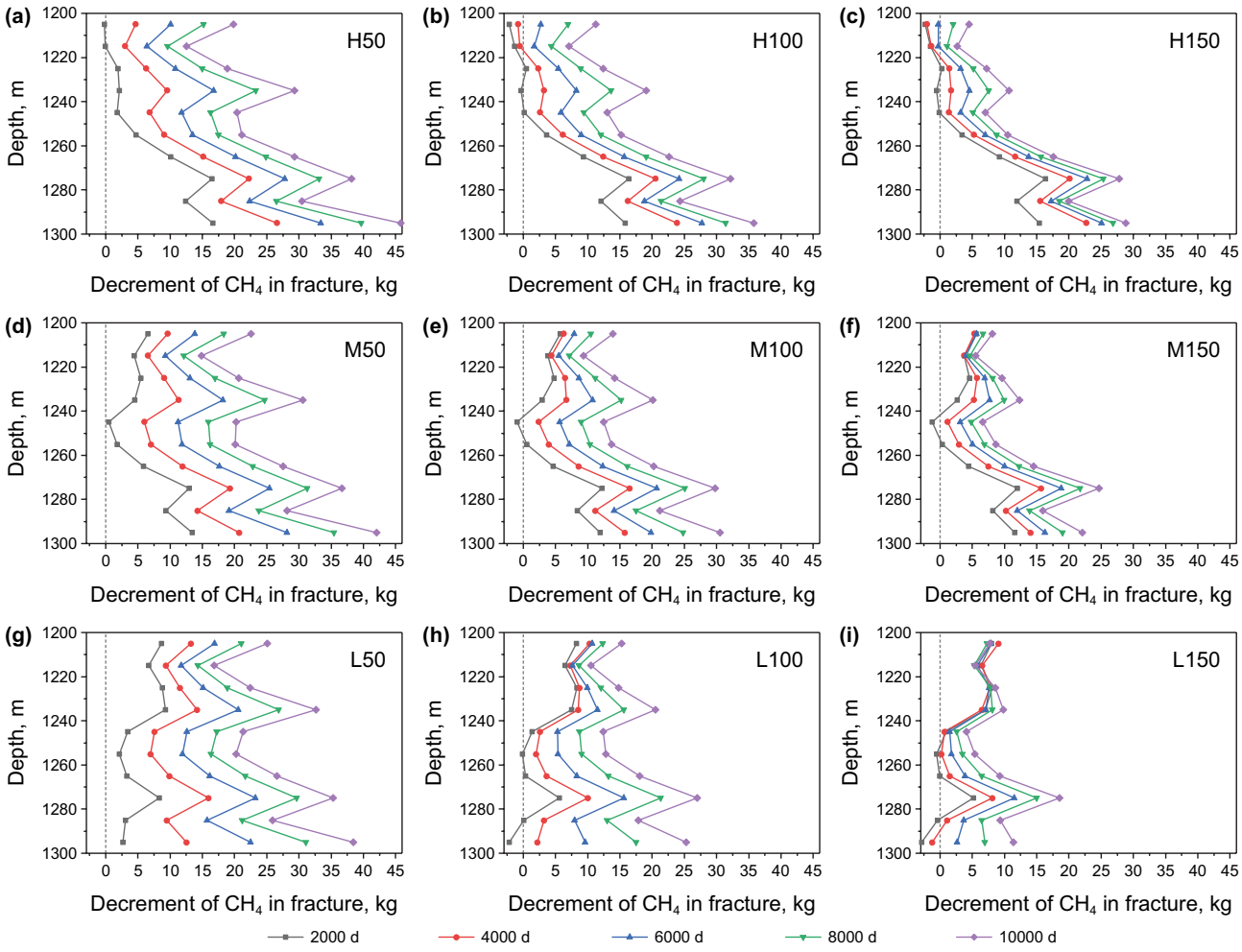

Fig. 6 Decrement of free CH_4 in fracture during the CS-EGR process for different IW–PWs combos

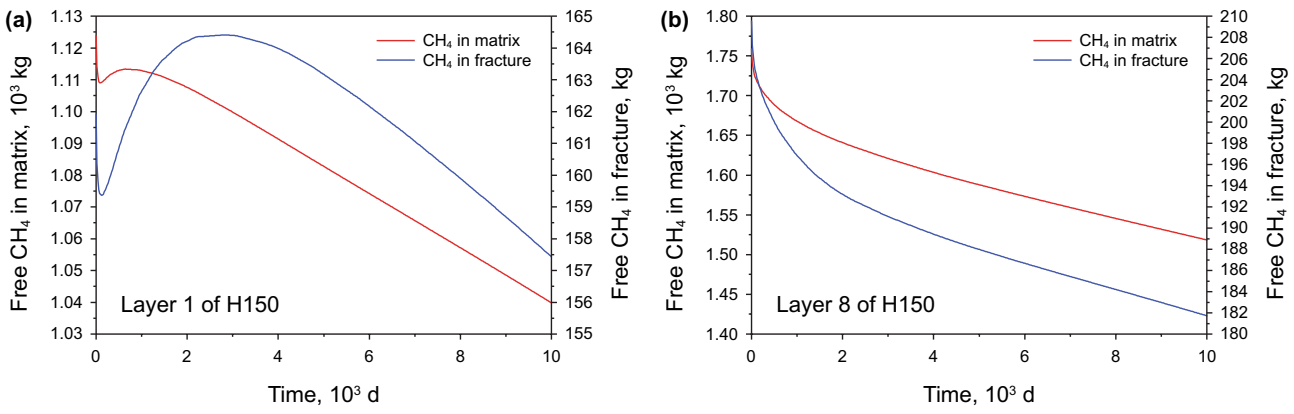

Fig. 7 Content variation of free CH_4 in different layers for H150

all IW–PWs combos (Fig. 8). Basically, the CH_4 content in the matrix at a depth of 1275 m (layer 8) decreases more than that in the rest of the layers, probably because the highest content of the original free CH_4 in the matrix (Fig. 3) and the highest permeability (Fig. 1) promotes the CH_4 release from the bottom PW in layer 8. When IW

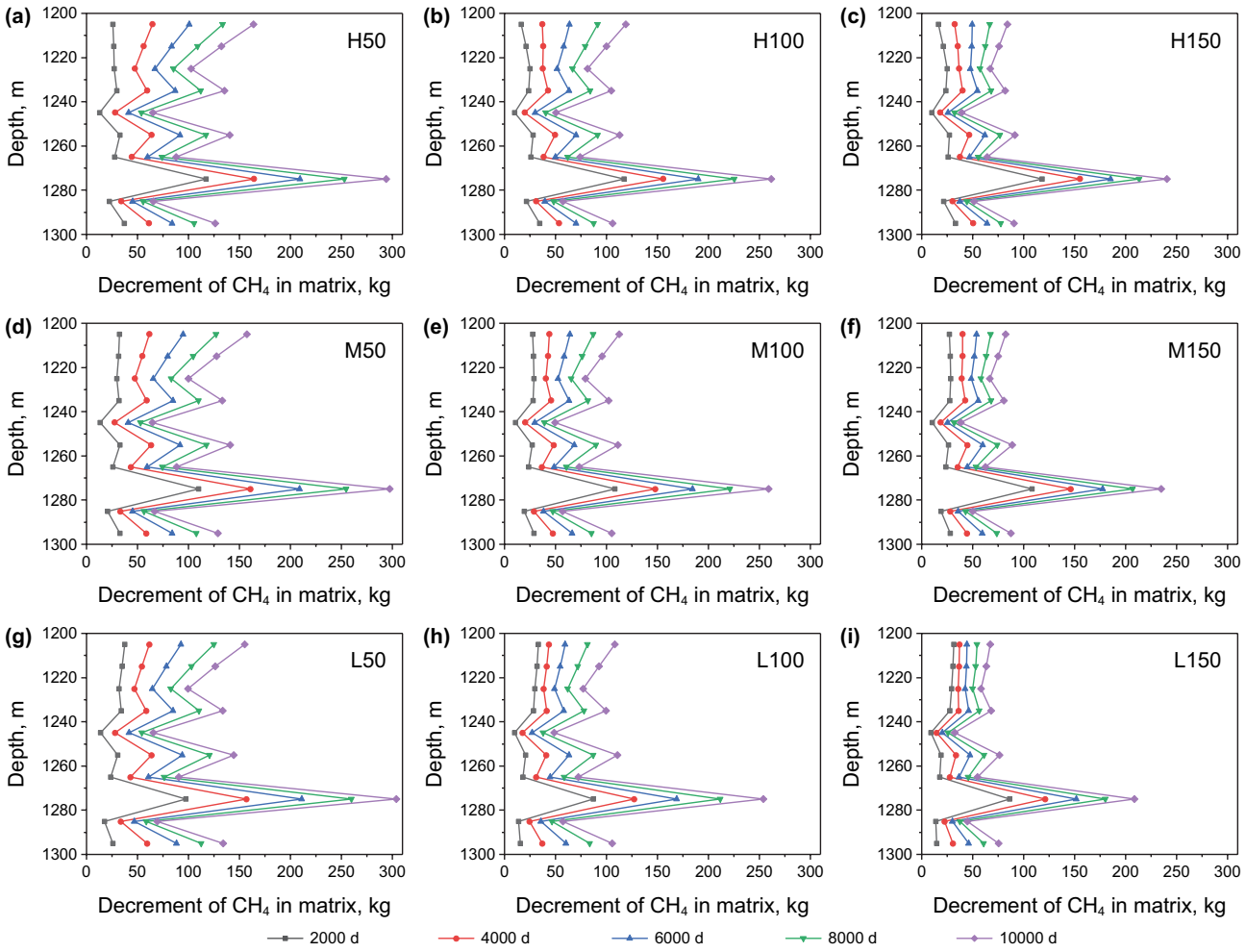

Fig. 8 Decrement of free CH_4 in the matrix during the CS-EGR process for different IW–PWs combos

has a fixed location, the content decrement of free CH_4 in the matrix at a shorter horizontal distance of IW–PWs is greater than that for a longer one. By comparison, the IW location only marginally affects the performance of free CH_4 in the matrix in a fixed situation of PWs, where an IW at the bottom layer makes the decrement of CH_4 content become slightly less than that at the upper layer (Fig. 8). Besides, no matter where the IW and PWs are, the content of free CH_4 in the matrix is invariably greater than that in the fracture during the CS-EGR process, in that the matrix porosity φ_m is considerably higher than the fracture porosity φ_f. This phenomenon is illustrated by the examples L150 and M100, where the ratio of CH_4 in the matrix relative to that in the fracture decrease rapidly, then slow by after CO_2 involvement, which however is always greater than 1 (Fig. 9). Figure 9 also indicates this dynamic ratio of CH_4 in the matrix to CH_4 in the fracture differs under different IW–PWs patterns, in which the detailed mechanism will be described in future work.

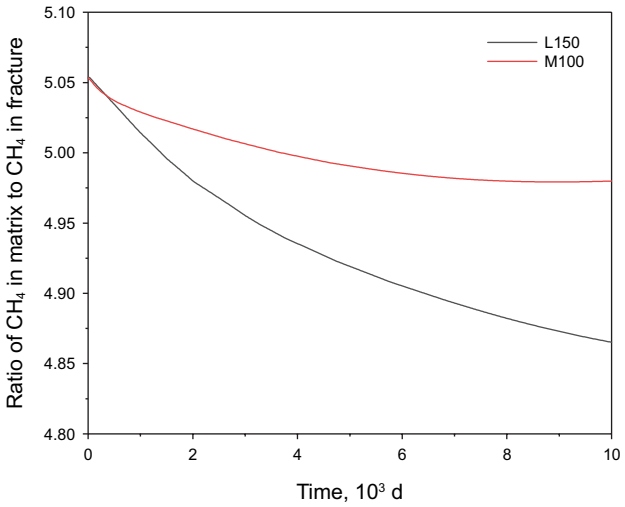

Fig. 9 CO_2 injection-induced variation of the ratio of CH_4 in the matrix relative to that in the fracture during the CS-EGR process

4.2 Content variation of free CO_2 during shale-based CS-EGR process

As exhibited by the representative case M100, the mass content and distribution area of the free CO_2 in the reservoir gradually become greater with time after CO_2 is injected into the Wufeng–Longmaxi shale (Fig. 4c, d). Here, the variation is characterized as heterogeneous in the vertical direction, in which the performance of free CO_2 in the fracture differs from that in the matrix. This heterogeneous variation leads to the variable outcomes of free CO_2 content, either in the fracture or in the matrix during 10,000 d of CS-EGR operation, under different relative locations of IW–PWs (Fig. 5c, d). From the qualitative perspective, after 10,000 d of CO_2 injection, the free CO_2 tends to be trapped more at a longer IW–PWs distance with a fixed IW location, while a bottom IW location enables more CO_2 in the free phase to be trapped than an upper one. Herein, this phenomenon is general and is suitable for the free CO_2, both in the fracture and in the matrix (Fig. 5c, d).

During the CS-EGR process, the fracture is the first space in the shale reservoir to encounter the injected CO_2; therefore, the relative locations of IW and PWs significantly affect the performance of free CO_2 in the fracture, as shown by the numerical outputs of every single layer (Fig. 10). For all IW–PWs combos, the layers close to the IW meet the CO_2 first and tend to trap more CO_2 in the fracture. For example, a 2000 d of CS-EGR operation enables a considerable amount of free CO_2 to be trapped in layers 8–10 but less free CO_2 to be trapped in layers 1–3 in the case L50; furthermore, after CO_2 is injected for 10,000 d, the content of free CO_2 in the fracture of layers 8–10 is obviously more than that of rest layers, for the example of case L50 (Fig. 10g). Besides, it is also noted that a longer IW–PWs distance allows more free CO_2 to be trapped in the fracture of each layer than a shorter one, when the IW is fixed (Fig. 10). This is due to a longer path for the CO_2 migration that usually corresponds to a greater area for CO_2 accumulation in the fracture.

As for the free CO_2 in the matrix, its content in each layer is variable during the process of CO_2 injection, under all

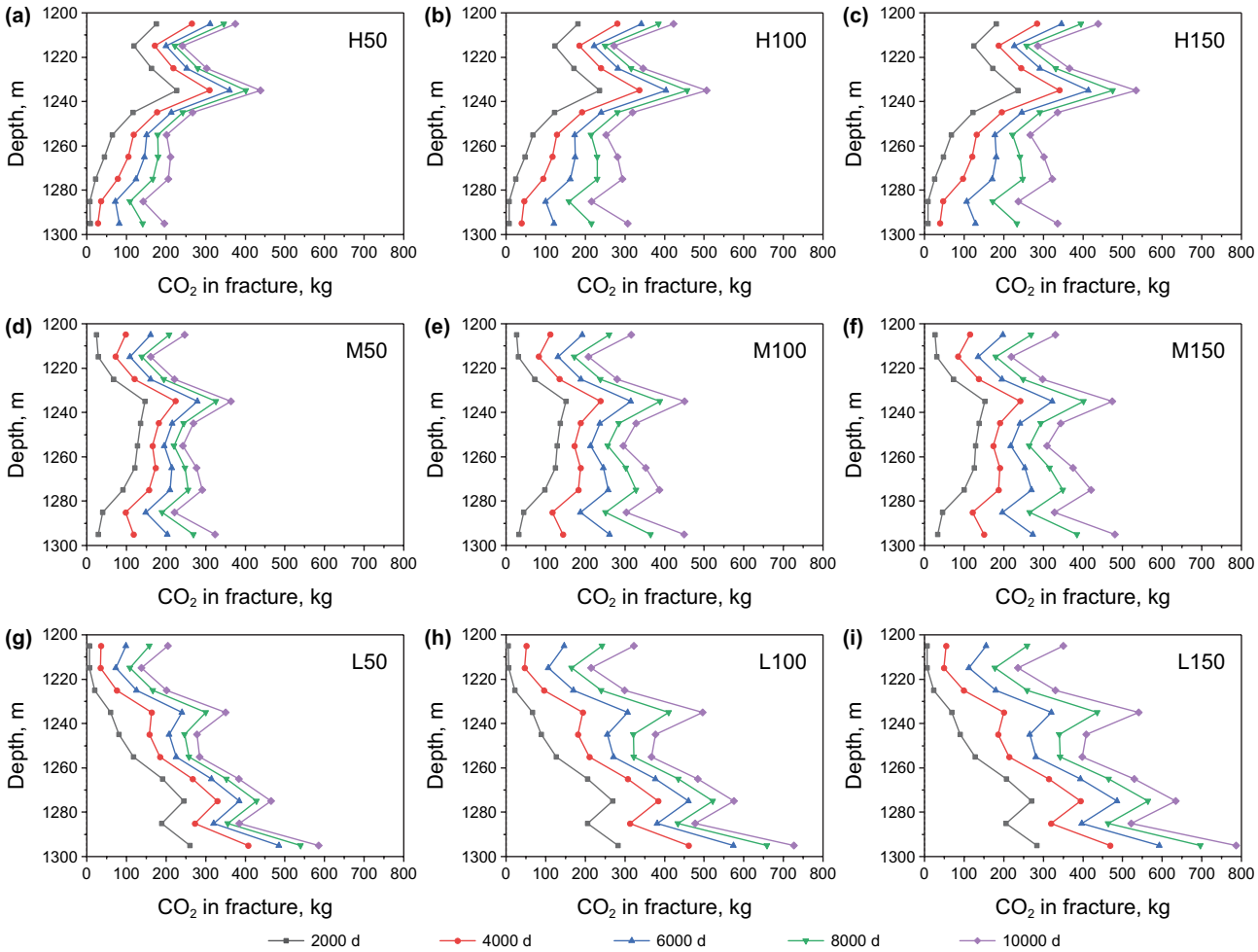

Fig. 10 Accumulation of free CO_2 in the fracture during the CS-EGR process for different IW–PWs combos

IW–PWs combos (Fig. 11). At first glance, for all IW–PWs situations, the matrix of layer 8 (depth of about 1275 m) performs effectively in the CO_2 trapping among all layers (Fig. 11), a result of the significant matrix porosity φ_m of layer 8 when compared with other layers (Fig. 1). In addition, the IW location affects the accumulation of free CO_2 in the matrix at a fixed situation of PWs, where the layers near the IW are likely to trap more free CO_2 in the matrix—similar to the effect for free CO_2 in the fracture. While for the situation of the fixed IW location, a longer IW–PWs distance makes more free CO_2 accumulated in the matrix, which is similar to the performance of free CO_2 in the fracture, with similar reasoning (Fig. 11).

Because the matrix porosity φ_m is significantly greater than the fracture porosity φ_f, for each layer, the content of free CO_2 in the matrix is higher than that in the fracture, revealed by Figs. 10 and 11. Quantitatively, the examples of H50 and M100 indicate that the ratio of free CO_2 in the matrix relative to that in the fracture is invariably superior during the whole CS-EGR process (Fig. 12). Nonetheless,

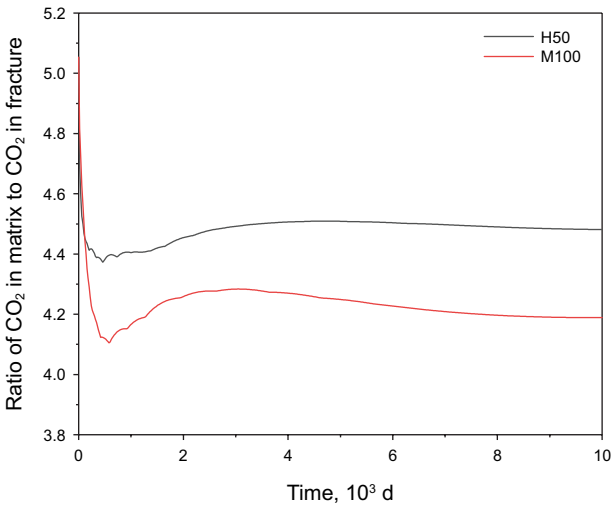

Fig. 12 Ratio of CO_2 in the matrix to that in the fracture after CO_2 injection during the CS-EGR process

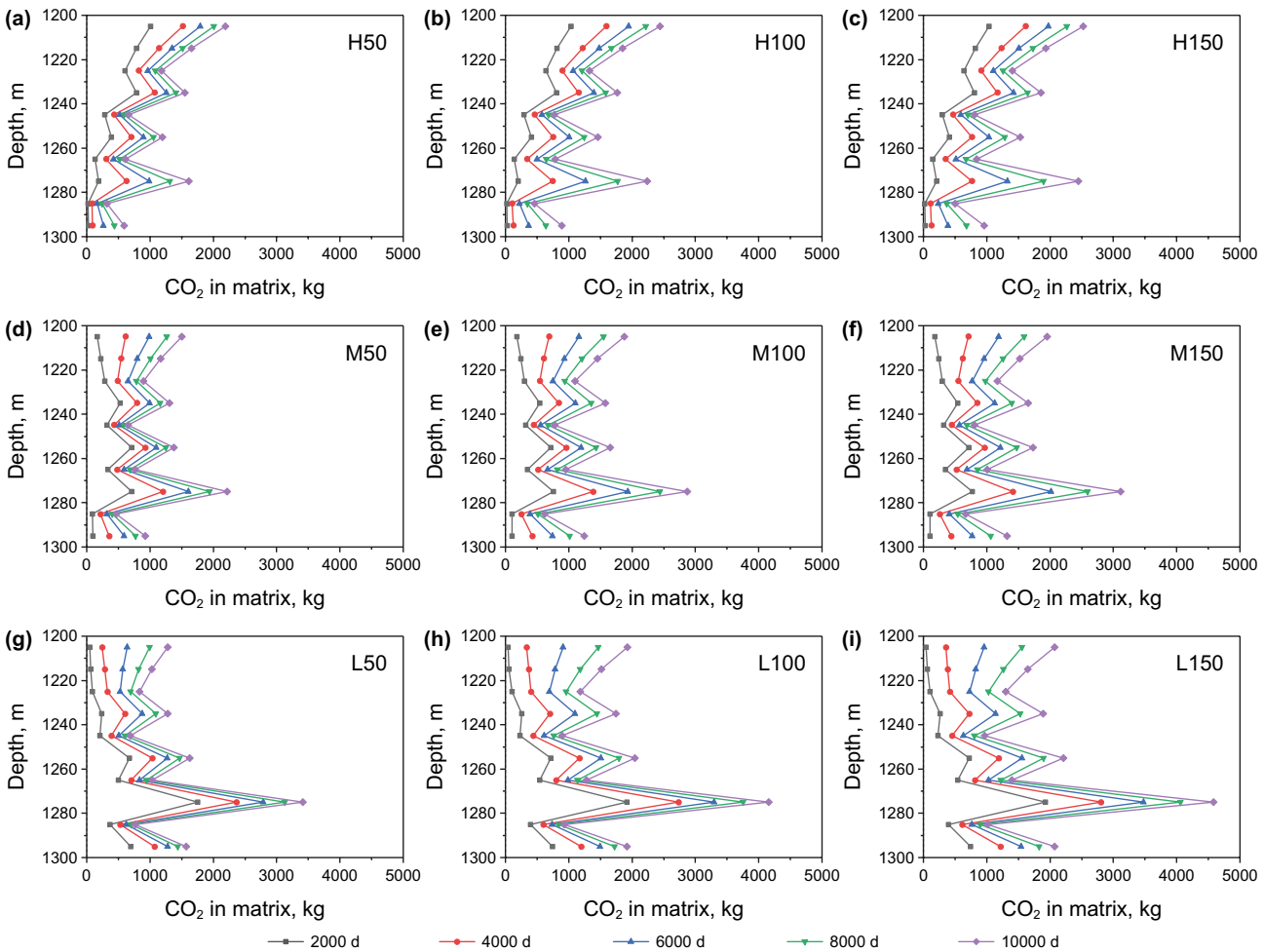

Fig. 11 Accumulation of free CO_2 in the matrix during the CS-EGR process for different IW–PWs combos

in Fig. 12, a sharp decline occurs in the very initial period of CO_2 injection, resulting from the injected CO_2 mainly staying in the fracture before arriving in the matrix pores; afterwards, this ratio has a small increase after CO_2 enters into the matrix pores of shale reservoir, and then tends to be stable.

4.3 Interactive behavior of free CO_2–CH_4 during the shale-based CS-EGR process

In the process of CS-EGR operation, the behavior of free gases is complex. For example, the free CH_4 in the matrix after CO_2 injection contains the original free CH_4 in the matrix and the desorbed CH_4 (originally in adsorbed) by CO_2 displacement. So, the interactive behavior between the free CO_2 and the free CH_4 is dynamic and complicated during the CS-EGR process in the shale reservoir. In Fig. 13, the content variation of free CH_4 and CO_2 echoes the outputs shown by Fig. 5, implicating the intensified impact on the performance of free gases from the relative locations of IW and PWs. Overall, the injection of CO_2 into the Wufeng–Longmaxi shale allows the content of free CH_4 and free CO_2 in the reservoir to decrease and increase, respectively (Fig. 13). Although the tendency of content variation for free CH_4 and free CO_2 is opposite, there are some common elements; for instance, the residual free CH_4 and trapped free CO_2 for case L150 are the greatest, while those for H50/M50 are the lowest (Fig. 13).

According to the statistics, the content fraction of free CH_4 among all free gases both in the fracture and in the matrix gets a continuous decrease with time, during the CS-EGR operation in the depleted Wufeng–Longmaxi shale (Fig. 14). Therein, the fraction of free CH_4 content in the fracture is consistently lower than that in the matrix, on the basis of two representative examples (Fig. 14). This phenomenon possibly is due to the extracted CH_4 from the PWs containing the free CH_4 in the fracture in the right side of the PWs (Fig. 4a), while the CH_4–CO_2 displacement that partly supplies the free CH_4 in the matrix mainly exists in the left side of PWs (Fig. 4). However, this hypothesis needs more

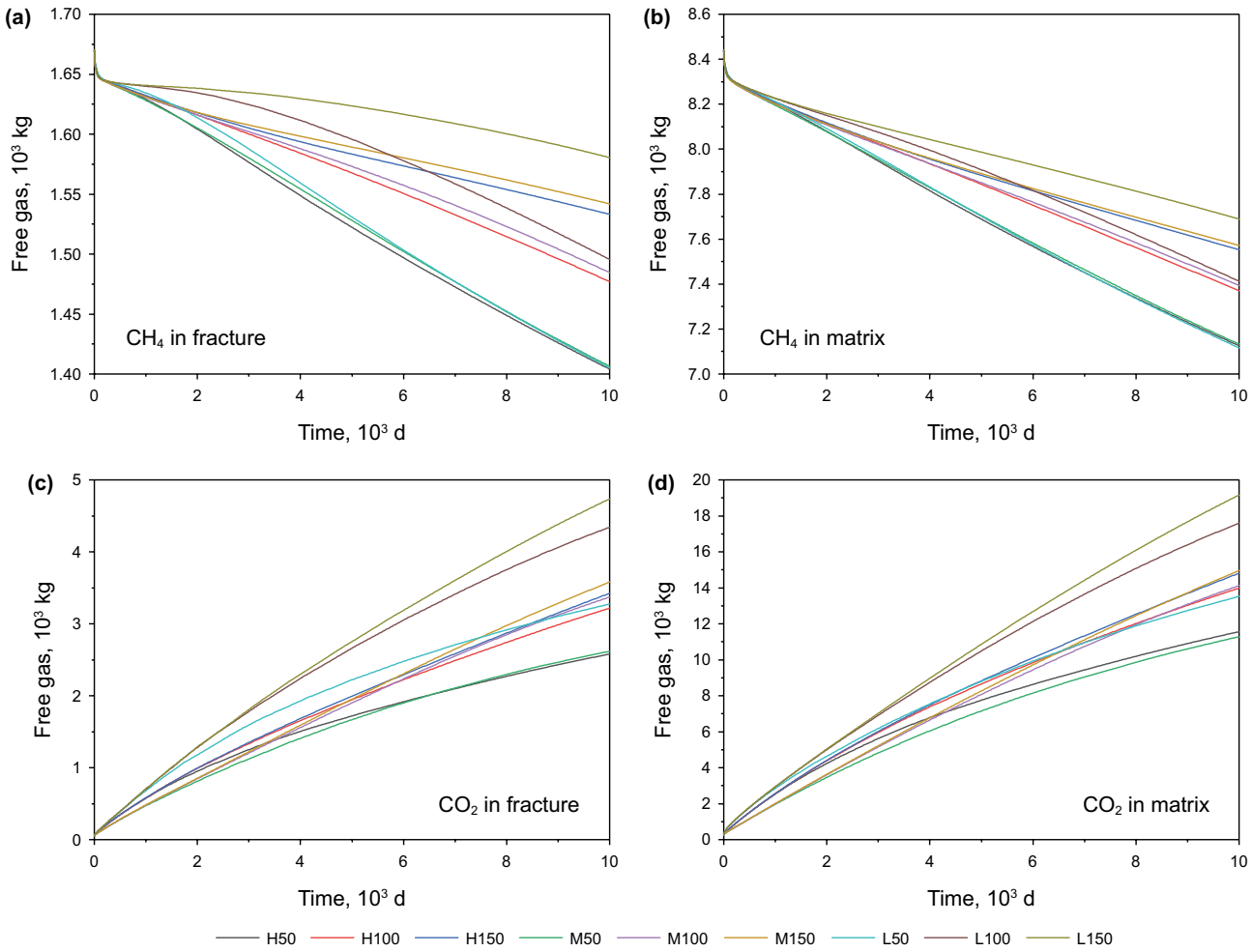

Fig. 13 Content variation of free CH_4 and CO_2 during the whole CS-EGR process

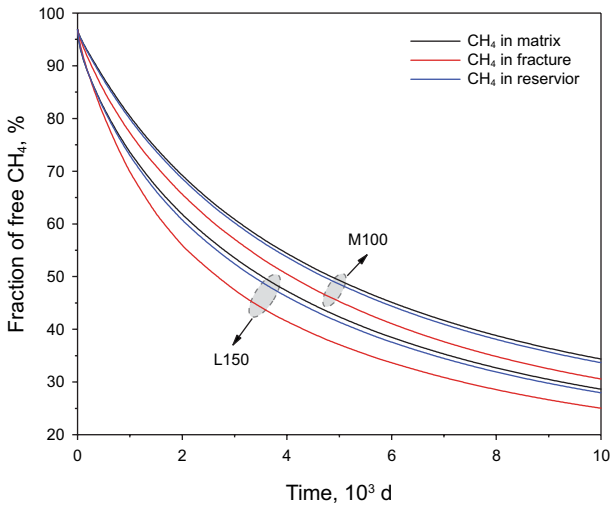

Fig. 14 Fraction of free CH_4 among all free gases (CH_4 and CO_2) for examples L150 and M100 during the CS-EGR process

attention. In addition, the variable fraction of free CH_4 in the fracture and that in the matrix together form the content fraction of free CH_4 relative to all free gases in the whole shale reservoir. Herein, reflected by the slope of change curves, the decreasing tendencies in Fig. 14 are of the "fast followed by slow" type, which suggests the proportion of free CH_4 among all free gases has a tendency to be constant after a sufficient time of CO_2 injection. Therefore, it can be speculated that the CS-EGR operation probably ends when the fraction of free CH_4 among all free gases changes insignificantly with time. Furthermore, after a 10,000 d of CS-EGR production, the resulting proportion of free CH_4 and free CO_2 differs, under different IW–PWs combos (Fig. 15). For all cases, no matter whether in the fracture or the matrix, the content of free CO_2 is primarily greater than that of free CH_4. After the CS-EGR operation runs for 10,000 d, for all IW–PWs combos, the content proportions of free CO_2 among all free gases in the matrix, the fracture and the whole reservoir are 65.8%, 69.5%, and 66.6% on average, respectively. Comparatively, it seems that a shorter IW–PWs distance (cases H50, M50 and L50) tends to enable a relatively higher proportion of free CH_4 both in the fracture and in the matrix, and thus in the whole reservoir (Fig. 15).

4.4 Location selection of IW–PWs for desired performance of free CO_2–CH_4

Since different IW–PWs locations facilitate variable interactive behavior of free CO_2 and free CH_4 during the shale-based CS-EGR process, it is necessary to make an appropriate selection on the relative locations of IW and PWs to achieve the desired purpose. For this selection, a parameter called the recovery efficiency of free CH_4 ($f_{\text{free-CH}_4}$, for short) is defined,

$$f_{\text{free-CH}_4} = \frac{C_o - C_r}{C_o} \times 100\% \quad (1)$$

where C_o and C_r are the content of the original free CH_4 (before CO_2 involvement) and the residual free CH_4 (after CO_2 involvement) in the fracture/matrix, respectively, kg.

Herein, a higher $f_{\text{free-CH}_4}$ value indicates that more CH_4 in the free phase is recovered from PWs, and vice versa. As exhibited in Fig. 16, the vertical heterogeneity is shown in the $f_{\text{free-CH}_4}$ value under each IW–PWs combo, during the CS-EGR operation in the Wufeng–Longmaxi shale, which is codetermined by the reservoir properties and the IW–PWs strategy. For all IW–PWs cases, the vertical heterogeneity of $f_{\text{free-CH}_4}$ has a similar relation to that of the free CH_4 in the matrix; that is, the $f_{\text{free-CH}_4}$ for bottom layers is higher than that for the upper layers (Fig. 16). With regard to the free CH_4 in the fracture, the $f_{\text{free-CH}_4}$ is affected by the IW location, and when the IW locates at the upper layers (or bottom layers), the $f_{\text{free-CH}_4}$ of bottom layers (or upper layers) becomes higher (Fig. 16).

The performance of free CH_4/CO_2 in the whole reservoir consists of that in the fracture and in the matrix of each layer. Basically, a longer IW–PWs distance generates

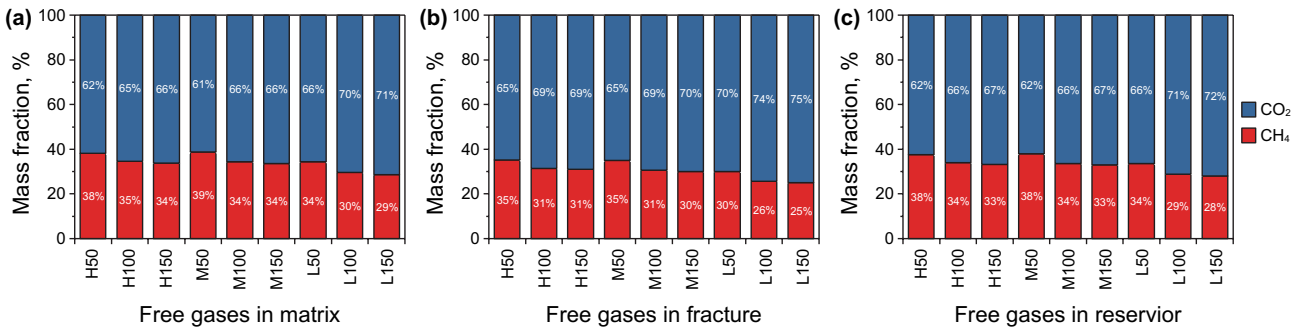

Fig. 15 Proportion of free CH_4 and free CO_2 in the Wufeng–Longmaxi shale after 10,000 d of CS-EGR operation

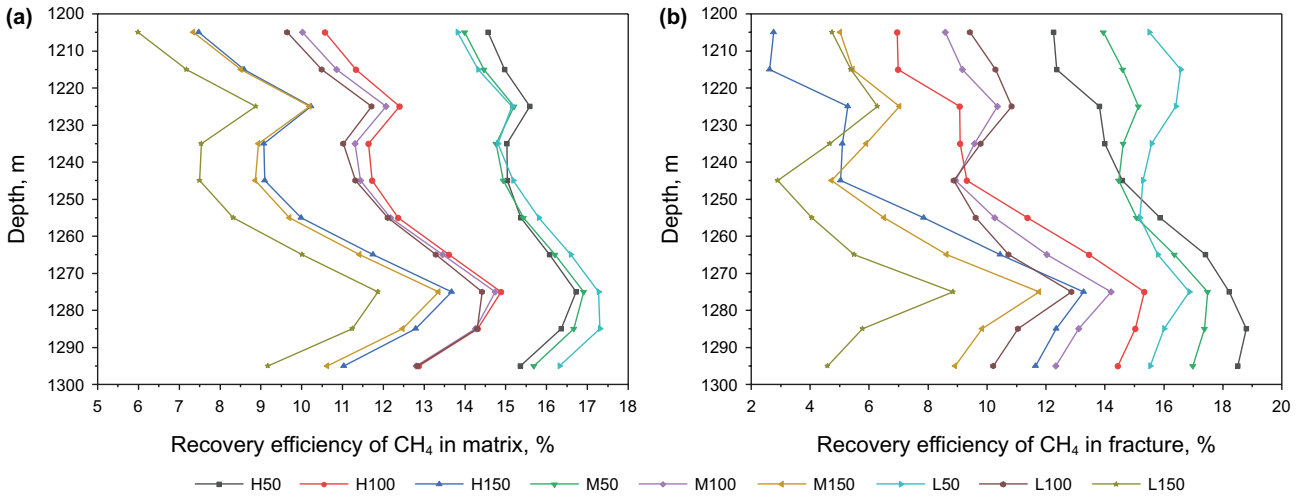

Fig. 16 Recovery efficiency of free CH_4 after 10,000 d of CO_2 injection into the Wufeng–Longmaxi shale

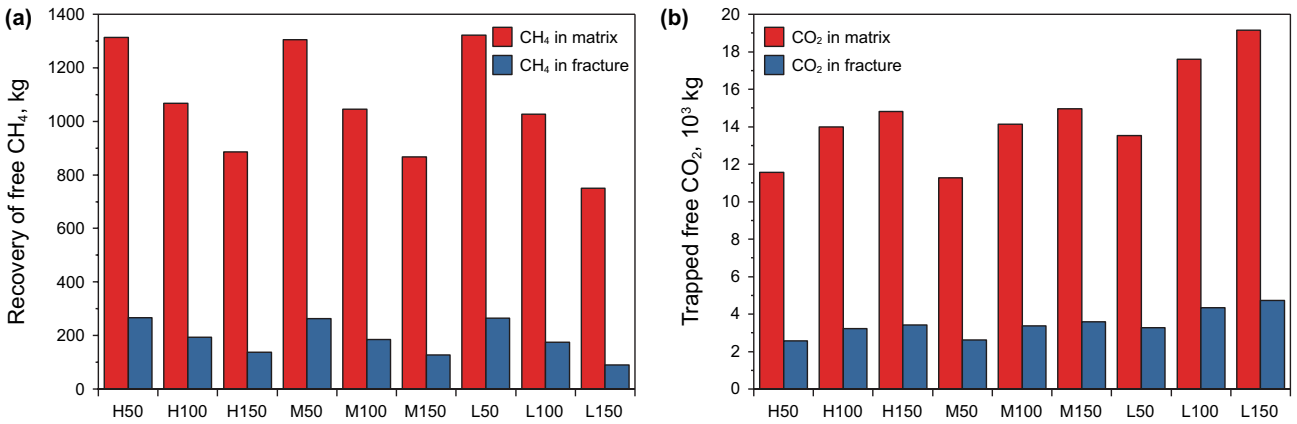

Fig. 17 Recovered free CH_4 and trapped free CO_2 in the Wufeng–Longmaxi shale after 10,000 d of CS-EGR operation

a lower recovered content of free CH_4 (Fig. 17a), accompanied with a higher trapped content of free CO_2 (Fig. 17b), both in the fracture and the matrix. Accordingly, an appropriate IW–PWs strategy can be selected for different expected targets. For example, if the CS-EGR operation aims to trap more CO_2 in the free phase in the depleted Wufeng–Longmaxi shale, the IW should be located in the bottom layers and have a longer horizontal distance with the PWs (like L150 in this work) (Fig. 17). One more example, if the CS-EGR operation is designed to get more CH_4 in the free phase recovered from the depleted Wufeng–Longmaxi shale, the IW location is flexible and only a shorter IW–PWs distance is needed, such as H50, M50, and L50 in this work (Fig. 17).

5 Conclusions

In developing a novel THM coupling model, the performance of free CH_4 and free CO_2 during the CS-EGR process in the Wufeng–Longmaxi shale is clearly obtained. The main conclusions are.

Vertical heterogeneity exists in the content of free CH_4 or free CO_2 in the fracture/matrix throughout the whole process of CS-EGR operation, codetermined by the reservoir properties and the IW–PWs strategy. Because the matrix porosity φ_m is significantly higher than the fracture porosity φ_f, the free CH_4/CO_2 in the matrix is much higher than that in the fracture for either layer or the whole

reservoir. After CO_2 involvement, the ratio of free CH_4/CO_2 in the matrix relative to that in the fracture declines and tends to be stable with time, where the change behavior is different for the free CH_4 and free CO_2.

For the free CH_4 in the fracture/matrix, its recovery is lower at a longer IW–PWs distance (fixed IW location) and is insignificantly affected by the variation of IW location at a PW location during the CS-EGR operation. For the free CO_2 in the fracture/matrix, it is trapped more at a longer IW–PWs distance (fixed IW location) and tends to be more trapped when the IW locates at bottom layers (fixed location of PWs). After CO_2 is injected into the Wufeng–Longmaxi shale, the free CH_4 content in the fracture/matrix of the layers near the IW location increases first and decreases later, while that of the layers far away from the IW location suffers a monotonic decrease.

During the CS-EGR operation in the Wufeng–Longmaxi shale, the content of free CH_4 among all free gases in the fracture/matrix has a continuous decline with time—in a "fast followed by slow" way. A 10,000 d of CO_2 injection enables the content of free CO_2 to be greater than that of free CH_4 in the fracture/matrix, in which a shorter IW–PWs distance results in a relatively higher proportion of free CH_4. In addition, when the IW locates at the bottom layers and has a farther distance to PWs, more CO_2 in the free phase tends to be trapped in the depleted Wufeng–Longmaxi shale; furthermore, no matter where the IW is, a shorter IW–PWs distance is helpful for getting more CH_4 in the free phase recovered from the depleted Wufeng–Longmaxi shale.

Acknowledgements This study was financially supported by the National Natural Science Foundation of China (Grant Nos. 51704197 and 11872258).

Compliance with ethical standards

Conflict of interest The authors declare that they have no known conflict of interest or personal relationships that could influence the work reported in this paper.

Open Access This article is licensed under a Creative Commons Attribution 4.0 International License, which permits use, sharing, adaptation, distribution and reproduction in any medium or format, as long as you give appropriate credit to the original author(s) and the source, provide a link to the Creative Commons licence, and indicate if changes were made. The images or other third party material in this article are included in the article's Creative Commons licence, unless indicated otherwise in a credit line to the material. If material is not included in the article's Creative Commons licence and your intended use is not permitted by statutory regulation or exceeds the permitted use, you will need to obtain permission directly from the copyright holder. To view a copy of this licence, visit http://creativecommons.org/licenses/by/4.0/.

Appendix

Key parameters for CS-EGR in this numerical simulation.

Parameter	Value
Langmuir strain coefficient of CH_4 ε_{L1}	8.1e−4
Langmuir strain coefficient of CO_2 ε_{L2}	3.6e−3
Dynamic viscosity of CH_4 μ_{g1}, Pa s	1.34e−5
Dynamic viscosity of CO_2 μ_{g2}, Pa s	1.84e−5
Dynamic viscosity of water μ_w, Pa s	8.9e−4
Diffusion coefficient of CH_4 D_1, m^2/s	3.6e−12
Diffusion coefficient of CO_2 D_2, m^2/s	5.8e−12
Thermal coefficient of gas sorption c_1, 1/K	0.021
Thermal coefficient of gas sorption c_2, 1/MPa	0.071
Capillary pressure p_{cgw}, MPa	0.035
Initial density of saturated vapor ρ_{fv0}, kg/m^3	0.13
Latent heat of vapor R_v, J/(K·kg)	461.51
Klinkenberg factor b_k, MPa	0.76
Desorption time of CH_4 τ_1, d	0.221
Desorption time of CO_2 τ_2, d	0.334
Henry's coefficient of CH_4 H_{g1}	0.0014
Henry's coefficient of CO_2 H_{g2}	0.0347
Residual gas saturation s_{gr}	0.05
Irreducible water saturation s_{wr}	0.42
Reference temperature for test T_{ref}, K	300
Endpoint relative permeability of gas k_{rg0}	0.875
Endpoint relative permeability of water k_{rw0}	1.0
Biot coefficient of matrix α_m	0.8
Biot coefficient of fracture α_f	0.1
Density of the shale skeleton ρ_c, kg/m^3	2470
Initial fracture width b, m	5e−4
Initial fracture stiffness K_{nj}, GPa/m	10
Maximum fracture aperture Δv_{max}, m	0.001
Thermal expansion coefficient α_T, 1/K	2.4e−5
Specific heat capacities of shale C_s, J/(kg K)	1380
Specific heat capacities of CH_4 C_{g1}, J/(kg K)	2220
Specific heat capacities of CO_2 C_{g2}, J/(kg K)	844
Specific heat capacities of water C_w, J/(kg K)	4187
Specific heat capacities of vapor C_v, J/(kg K)	1996
Thermal conduction coefficient of shale λ_s, W/(m K)	0.1913
Thermal conduction coefficient of CH_4 λ_{g1}, W/(m K)	0.0301
Thermal conduction coefficient of CO_2 λ_{g2}, W/(m K)	0.0137
Thermal conduction coefficient of water λ_w, W/(m K)	0.5985
Isosteric heat of CH_4 adsorption q_{st1}, kJ/mol	16.4
Isosteric heat of CO_2 adsorption q_{st2}, kJ/mol	19.2

References

Abidoye LK, Khudaida KJ, Das DB. Geological carbon sequestration in the context of two-phase flow in porous media: a review.

Crit Rev Environ Sci Technol. 2015;45(11):1105–47. https://doi.org/10.1080/10643389.2014.924184.

Ajayi T, Gomes JS, Bera A. A review of CO_2 storage in geological formations emphasizing modeling, monitoring and capacity estimation approaches. Pet Sci. 2019;16:1028–63. https://doi.org/10.1007/s12182-019-0340-8.

Bandis SC, Lumsden AC, Barton NR. Fundamentals of rock joint deformation. Int J Rock Mech Min Sci Geomech Abstr. 1983;20(6):249–68. https://doi.org/10.1016/0148-9062(83)90595-8.

Chen B, Harp DR, Lu Z, et al. Reducing uncertainty in geologic CO_2 sequestration risk assessment by assimilating monitoring data. Int J Greenh Gas Control. 2020;94:102926. https://doi.org/10.1016/j.ijggc.2019.102926.

Chi J, Ju B, Lv G, et al. A computational method of critical well spacing of CO_2 miscible and immiscible concurrent flooding. Pet Explor Dev. 2017;44(5):771–8. https://doi.org/10.1016/s1876-3804(17)30092-7.

Dahaghi AK. Numerical simulation and modeling of enhanced gas recovery and CO_2 sequestration in shale gas reservoirs: a feasibility study. In: SPE international conference on CO_2 capture, storage, and utilization, 10–12 November, New Orleans, Louisiana, USA. Society of Petroleum Engineers. 2010. https://doi.org/10.2118/139701-MS.

Du X, Gu M, Hou Z, et al. Experimental study on kinetics of adsorption of CO_2 and CH_4 in gas-bearing shale reservoirs. Energy Fuel. 2019;33(12):12587–600. https://doi.org/10.1021/acs.energyfuels.9b03176.

Fan C, Elsworth D, Li S, et al. Thermo-hydro-mechanical–chemical couplings controlling CH_4 production and CO_2 sequestration in enhanced coalbed methane recovery. Energy. 2019a;173:1054–77. https://doi.org/10.1016/j.energy.2019.02.126.

Fan C, Li S, Elsworth D, et al. Experimental investigation on dynamic strength and energy dissipation characteristics of gas outburst-prone coal. Energy Sci Eng. 2019b;8(4):1015–28. https://doi.org/10.1002/ese3.565.

Fan C, Luo M, Li S, et al. A thermo-hydro-mechanical–chemical coupling model and its application in acid fracturing enhanced coalbed methane recovery simulation. Energies. 2019c;12(4):626. https://doi.org/10.3390/en12040626.

Fathi E, Akkutlu IY. Multi-component gas transport and adsorption effects during CO_2 injection and enhanced shale gas recovery. Int J Coal Geol. 2014;123:52–61. https://doi.org/10.1016/j.coal.2013.07.021.

Iddphonce R, Wang J, Zhao L. Review of CO_2 injection techniques for enhanced shale gas recovery: Prospect and challenges. J Nat Gas Sci Eng. 2020;77:103240. https://doi.org/10.1016/j.jngse.2020.103240.

Ji W, Song Y, Jiang Z, et al. Estimation of marine shale methane adsorption capacity based on experimental investigations of Lower Silurian Longmaxi formation in the Upper Yangtze Platform, south China. Mar Pet Geol. 2015;68:94–106. https://doi.org/10.1016/j.marpetgeo.2015.08.012.

Kalra S, Tian W, Wu X. A numerical simulation study of CO_2 injection for enhancing hydrocarbon recovery and sequestration in liquid-rich shales. Pet Sci. 2018;15:103–15. https://doi.org/10.1007/s12182-017-0199-5.

Li D, He Y, Zhang H, et al. A numerical study of the impurity effects on CO_2 geological storage in layered formation. Appl Energy. 2017;199:107–20. https://doi.org/10.1016/j.apenergy.2017.04.059.

Li R, Dong S, Dan L, et al. Tectonically driven organic fluid migration in the Dabashan Foreland Belt: evidenced by geochemistry and geothermometry of vein-filling fibrous calcite with organic inclusions. J Asian Earth Sci. 2013;75(8):202–12. https://doi.org/10.1016/j.jseaes.2013.07.026.

Li X, Elsworth D. Geomechanics of CO_2 enhanced shale gas recovery. J Nat Gas Sci Eng. 2015;26:1607–19. https://doi.org/10.1016/j.jngse.2014.08.010.

Li Z, Elsworth D. Controls of CO_2–N_2 gas flood ratios on enhanced shale gas recovery and ultimate CO_2 sequestration. J Pet Sci Eng. 2019;179:1037–45. https://doi.org/10.1016/j.petrol.2019.04.098.

Liu J, Yao Y, Zhu Z, et al. Experimental investigation of reservoir characteristics of the upper Ordovician Wufeng Formation shale in middle–upper Yangtze region, China. Energy Explor Exploit. 2016a;34(4):527–42. https://doi.org/10.1177/0144598716650553.

Liu J, Yao Y, Elsworth D, et al. Vertical heterogeneity of the shale reservoir in the Lower Silurian Longmaxi Formation: analogy between the southeastern and northeastern Sichuan Basin, SW China. Minerals. 2017a;7(8):151. https://doi.org/10.3390/min7080151.

Liu J, Yao Y, Liu D, et al. Experimental evaluation of CO_2 enhanced recovery of adsorbed-gas from shale. Int J Coal Geol. 2017b;179:211–8. https://doi.org/10.1016/j.coal.2017.06.006.

Liu J, Xie L, Elsworth D, et al. CO_2/CH_4 competitive adsorption in shale: implications for enhancement in gas production and reduction in carbon emissions. Environ Sci Technol. 2019a;53(15):9328–36. https://doi.org/10.1021/acs.est.9b02432.

Liu J, Xie L, Yao Y, et al. Preliminary study of influence factors and estimation model of the enhanced gas recovery stimulated by carbon dioxide utilization in shale. ACS Sustain Chem Eng. 2019b;7(24):20114–25. https://doi.org/10.1021/acssuschemeng.9b06005.

Liu J, Xie H, Wang Q, et al. Influence of pore structure on shale gas recovery with CO_2 sequestration: insight into molecular mechanisms. Energy Fuel. 2020;34(2):1240–50. https://doi.org/10.1021/acs.energyfuels.9b02643.

Liu Y, Zhang J, Tang X. Predicting the proportion of free and adsorbed gas by isotopic geochemical data: a case study from lower Permian shale in the southern North China basin (SNCB). Int J Coal Geol. 2016b;156:25–35. https://doi.org/10.1016/j.coal.2016.01.011.

Ma D, Duan H, Zhang Q, et al. A numerical gas fracturing model of coupled thermal, flowing and mechanical effects. CMC Comput Mater Continua. 2020;65(3):2123–41. https://doi.org/10.32604/cmc.2020.011430.

Meng Q, Zhang G. Geologic framework and tectonic evolution of the Qinling orogen, central China. Tectonophysics. 2000;323(3–4):183–96. https://doi.org/10.1016/s0040-1951(00)00106-2.

Mohagheghian E, Hassanzadeh H, Chen Z. CO_2 sequestration coupled with enhanced gas recovery in shale gas reservoirs. J CO2 Util. 2019;34:646–55. https://doi.org/10.1016/j.jcou.2019.08.016.

Nassir M, Settari A, Wan RG. Prediction of stimulated reservoir volume and optimization of fracturing in tight gas and shale with a fully elasto-plastic coupled geomechanical model. SPE J. 2014;19(5):771–85. https://doi.org/10.2118/163814-PA.

Pan Y, Hui D, Luo P, et al. Experimental investigation of the geochemical interactions between supercritical CO_2 and shale: implications for CO_2 storage in gas-bearing shale formations. Energy Fuel. 2018;32(2):1963–78. https://doi.org/10.1021/acs.energyfuels.7b03074.

Rani S, Prusty BK, Pal SK. Characterization of shales from Damodar valley coalfields for CH_4 recovery and CO_2 sequestration. Environ Technol Innov. 2020;18:100739. https://doi.org/10.1016/j.eti.2020.100739.

Řimnáčová D, Weishauptová Z, Přibyl O, et al. Effect of shale properties on CH_4 and CO_2 sorption capacity in Czech Silurian shales. J Nat Gas Sci Eng. 2020. https://doi.org/10.1016/j.jngse.2020.103377.

Shi W, Zhang Y, Dong S, et al. Intra-continental Dabashan orocline, southwestern Qinling, Central China. J Asian Earth Sci. 2012;46:20–38. https://doi.org/10.1016/j.jseaes.2011.10.005.

Sun H, Yao J, Gao SH, et al. Numerical study of CO_2 enhanced natural gas recovery and sequestration in shale gas reservoirs. Int J Greenh Gas Control. 2013;19:406–19. https://doi.org/10.1016/j.ijggc.2013.09.011.

Tang X, Jiang Z, Jiang S, et al. Heterogeneous nanoporosity of the Silurian Longmaxi Formation shale gas reservoir in the Sichuan Basin using the QEMSCAN, FIB-SEM, and nano-CT methods. Mar Pet Geol. 2016;78:99–109. https://doi.org/10.1016/j.marpetgeo.2016.09.010.

Tao Z, Bielicki JM, Clarens AF. Physicochemical factors impacting CO_2 sequestration in depleted shale formations: the case of the Utica shale. Energy Procedia. 2014;63:5153–63. https://doi.org/10.1016/j.egypro.2014.11.545.

Wan T, Liu HX. Exploitation of fractured shale oil resources by cyclic CO_2 injection. Pet Sci. 2018;15(3):552–63. https://doi.org/10.1007/s12182-018-0226-1.

Wang G, Long S, Ju Y, et al. Application of horizontal wells in three-dimensional shale reservoir modeling: a case study of Longmaxi-Wufeng shale in Fuling gas field, Sichuan Basin. AAPG Bull. 2018;102(11):2333–54. https://doi.org/10.1306/05111817144.

Wang T, Tian S, Li G, et al. Molecular simulation of CO_2/CH_4 competitive adsorption on shale kerogen for CO_2 sequestration and enhanced gas recovery. J Phys Chem C. 2018;120(30):17009–18. https://doi.org/10.1021/acs.jpcc.8b02061.

Yao Y, Liu J, Liu D, et al. A new application of NMR in characterization of multiphase methane and adsorption capacity of shale. Int J Coal Geol. 2019;201:76–85. https://doi.org/10.1016/j.coal.2018.11.018.

Yang ZL, Yu HY, Chen ZW, et al. A compositional model for CO_2 flooding including CO_2 equilibria between water and oil using the Peng–Robinson equation of state with the Wong–Sandler mixing rule. Pet Sci. 2019;16:874–89. https://doi.org/10.1007/s12182-018-0294-2.

Ye YH, Liu SG, Ran B, et al. Characteristics of black shale in the Upper Ordovician Wufeng and lower Silurian Longmaxi formations in the Sichuan Basin and its periphery, China. Aust J Earth Sci. 2017;64:667–87. https://doi.org/10.1080/08120099.2017.1321581.

Zhang G, Zhou W, Ji S, et al. Experimental study on CO_2 replacement method used in shale gas exploration. J Chengdu Univ Technol. 2015;42(3):366–71 (**in Chinses**).

Zhang K, Jiang H, Qin G. Utilization of zeolite as a potential multifunctional proppant for CO_2 enhanced shale gas recovery and CO_2 sequestration: a molecular simulation study on the competitive adsorption of CH_4 and CO_2 in zeolite and organic matter. Fuel. 2019;249(1):119–29. https://doi.org/10.1016/j.fuel.2019.03.061.

Zhang H, Diao R, Mostofi M, et al. Monte Carlo simulation of the adsorption and displacement of CH_4 by CO_2 Injection in shale organic carbon slit micropores for CO_2 enhanced shale gas recovery. Energy Fuel. 2020;34(1):150–63. https://doi.org/10.1021/acs.energyfuels.9b03349.

Zhao P, Xie L, He B, et al. Strategy optimization on industrial CO_2 sequestration in the depleted Wufeng–Longmaxi formation shale in the northeastern Sichuan basin, SW China: from the perspective of environment and energy. ACS Sustain Chem Eng. 2020;8:11435–45. https://doi.org/10.1021/acssuschemeng.0c04114.

Zhou L, Su X, Lu Y, et al. A new three-dimensional numerical model based on the equivalent continuum method to simulate hydraulic fracture propagation in an underground coal mine. Rock Mech Rock Eng. 2018;52(8):213–33. https://doi.org/10.1007/s00603-018-1684-x.

Zhou J, Jin Z, Luo K. Effects of moisture contents on shale gas recovery and CO_2 sequestration. Langmuir. 2019;35(26):8716–25. https://doi.org/10.1021/acs.langmuir.9b00862.

Zhu Y, Wang X, Feng M, et al. Lithofacies classification and its relationship with reservoir of the Lower Paleozoic Wufeng–Longmaxi Formation in the eastern Sichuan Basin. Lithol Reserv. 2016;28(5):59–66 (**in Chinses**).